Additive Manufacturing 82 (2024) 104046

Contents lists available at ScienceDirect

Additive Manufacturing

journal homepage: www.elsevier.com/locate/addma

Analytical modelling of scanning strategy effect on temperature field and melt track dimensions in laser powder bed fusion

Pramod R. Zagade [a,b,*], B.P. Gautham [a], Amitava De [b], Tarasankar DebRoy [c]

[a] TCS Research, Tata Consultancy Services, Pune, India,
[b] Indian Institute of Technology Bombay, India,
[c] The Pennsylvania State University, University Park, PA, USA

ARTICLE INFO

Keywords:
Laser powder bed fusion (LPBF)
Spiral scanning
Circular beam oscillation scanning strategy
Thermal stress
Analytical heat transfer model

ABSTRACT

The manufacture of defect-free and dimensionally accurate parts in laser powder bed fusion (LPBF) is influenced by temperature field, deposited track geometry, and process-induced thermomechanical stress. The selection of an appropriate scanning strategy is key to achieving this goal. Well-tested numerical models of heat transfer and thermal stress are possible routes to design for the LPBF process, but these models are computationally expensive and arduous for practicing engineers. Here, we introduce an analytical heat transfer model tailored for part-scale LPBF simulations, encompassing widely used scanning strategies such as linear, circular, spiral, and circular beam oscillation paths. Notably, our model integrates exact curvilinear trajectories of the laser beam, enhancing fidelity in representing non-linear scanning paths. The computed melt track profiles and thermal cycles are tested rigorously with the corresponding experimentally measured independent results. The computational times for various scanning strategies are examined. A unique temperature non-uniformity metric is defined as the sum of the normalized deviations between the computed temperature field in a layer and the average layer temperature at any time instance. The computed temperature non-uniformity metric is shown to work well as a susceptibility factor for the thermal stress along a layer. Ultimately, the work underscores the potential of an efficient analytical heat transfer model, reducing trial-and-error tests and helping to select optimal scanning strategies in part-scale LPBF.

1. Introduction

The scanning strategy in laser powder bed fusion (LPBF) impacts the temperature field and, the thermomechanical stress and distortion of the final part [1–4]. Trial experiments are a common practice to find a suitable scanning strategy for a defect-free, structurally sound, and dimensionally accurate part [1,3,5]. Computer-based numerical models are routinely preferred for prior estimation of the temperature field, porosity [6,7], thermomechanical stress [8–11], and distortion [12] in LPBF. These models could reduce the volume of trial experiments to help design an effective scanning strategy. However, they are expensive, complex, and computationally intensive for part-scale. As a result, their use is often restricted to the simulation of only a few short tracks [7]. In contrast, analytical heat transfer models can predict the temperature field for several hundreds and thousands of tracks rapidly and with fair accuracy [13–15]. The analytical heat transfer models for LPBF available in the literature rarely considered the effect of the scanning strategy [16,17].

The scanning strategy in LPBF refers to the spatial path composed of several tracks that are followed by a fast-moving finely-focussed laser beam along a layer [4]. Different scanning strategies such as unidirectional, bidirectional, in-out and out-in spirals, and fractal are commonly followed [3,4]. Larimian et al. [18] reported an increase in the part density and microhardness with bidirectional scanning for LPBF of SS316L. Likewise, Valente et al. [19] achieved near full density build with bidirectional scanning for LPBF of Ti6Al4V. The bidirectional scanning strategy resulted in uniformly distributed residual stress for LPBF of CpTi [20] and Ti6Al4V [21]. For LPBF of SS316L, Bo et al. [22] reported a decrease in the thermomechanical distortion with an out-in spiral scanning compared to bidirectional scanning. A change in the scanning direction by 67° in alternate layers reduced lack-of-fusion and microcracks for LPBF of Hastelloy X [23]. Zhang et al. [24] reported an improvement in the surface quality and a decrease in the residual stresses with the decrease in the *island* size for LPBF of aluminum alloy. The impact of the scanning strategy on thermomechanical distortion and

* Corresponding author at: TCS Research, Tata Consultancy Services, Pune, India
E-mail address: pramod.zagade@tcs.com (P.R. Zagade).

https://doi.org/10.1016/j.addma.2024.104046
Received 7 October 2023; Received in revised form 5 February 2024; Accepted 12 February 2024
Available online 14 February 2024

Nomenclatures

α	Thermal diffusivity
β	Volumetric thermal expansion coefficient
C	Specific heat
δ	Hatch spacing
ε^*	Thermal strain parameter
EI	Flexural rigidity
η	Absorption coefficient
ν	Oscillation frequency
ϕ_s	Phase angle at the start of oscillating circle
f_p	Laser intensity distribution factor in planar direction
f_d	Laser intensity distribution factor in depth direction
F	Fourier number
h	Height of the volumetric heat source
H	Heat input per unit length
k	Thermal conductivity
k_0, C_0, m	Material constants
L_S	Scanning track length
n	Number scanning tracks
n_l	Number of points in a layer for ΔT calculation
N	Number of loops in the spiral path
P	Laser power
ρ	Density
r_b	Laser beam radius
r_c, r_p, r_o	Radius of circular, spiral and circular beam oscillation scanning tracks
S	Time to complete scanning of spiral path
t	Time
t^*	Deposition time
t_s	Starting time of the scanning track
t_e	Ending time of the scanning track
T	Temperature
T_0	Initial temperature of the substrate and powder bed
$\dot{T}$	Cooling rate
T_j	Temperature at j^{th} location in the layer
T_a	Average layer temperature
ΔT	Temperature non-uniformity
ΔT^*	Difference between peak and surrounding temperature
v	Scanning speed
v_c	Scanning speed in circular scanning track
v_x, v_y	Scanning speed in X and Y directions, respectively
x, y, z	Cartesian coordinates
x_c, y_c	Coordinates of center of circular track
x_o, y_o	Coordinates of center of circular beam oscillation scanning track
x_p, y_p	Coordinates of center spiral scanning track
x_s, y_s	Starting coordinates of a scanning track

stress was also examined for LPBF of IN718 [2,25,26], Ti6Al4V [5,27,28], H13 [29] and SS316L [9,30].

Computational models for LPBF use heat transfer analysis to predict the temperature field during the scanning of a few tracks and layers, followed by mechanical analysis to calculate the resultant stress distribution and distortion [31–35]. Numerical models often use lumped or aggregated heat input of multiple tracks and layers to estimate part scale temperature field and subsequently, predict residual stress and distortion in the part [36–42]. Numerical models for LPBF are also developed to examine the effect of the scanning strategy on temperature field [43,44], porosity [6,7], and residual stress and distortion [10–12]. Cao [7] used a heat transfer and fluid flow model to study the effect of scanning strategy on build porosity and surface roughness. Cheng et al. [45] used a thermomechanical analysis for LPBF of IN718 and reported minimum distortion and residual stress when the scanning tracks were inclined by 45° to the part boundary. A thermomechanical analysis by Parry et al. [11] for LPBF of Ti6Al4V showed a smaller residual stress for shorter scanning tracks. The aforementioned studies showed the ability of the computational models to help design a suitable scanning strategy but these models were restricted to simulate only a very few short tracks [6,7,45].

Analytical heat transfer models for LPBF are evolving and can undertake a rapid calculation of the temperature field [17], cooling rates [46], and susceptibility to lack-of-fusion porosity [47,48]. Current analytical heat transfer models for LPBF rarely account for the effect of the scanning strategy [16,17]. Moreover, with the advent of laser guiding systems, complex scanning strategies involving non-linear scanning tracks such as circular [49], trochoidal [50], continuous spiral [51], and circular beam oscillation [52,53] are being tested to reduce LPBF defects and enhance the part properties. The current analytical models treat the curved paths as a series of linear tracks [16,17] that introduce errors in the laser path description. As a recourse, a large number of independent linear tracks are needed to closely represent a curvilinear path, but it leads to an increase in computational time [17].

We report here the development and validation of an analytical heat transfer model for LPBF with commonly used scanning strategies such as linear, circular, and spiral paths. A well-tested analytical model for linear tracks [15] is enhanced extensively and exhaustively to simulate the laser beam scanning of non-linear and curvilinear paths with any given strategy. The computed results of temperature field, melt pool shapes and sizes, and thermal cycles for different scanning strategies are tested with the corresponding experimentally measured results from the literature. An assessment of the overall computational time and accuracy is presented to show the efficacy of the proposed analytical model. The computed temperature field is used to comprehend the effect of a scanning strategy on a uniquely defined temperature non-uniformity metric that shows a substantive potential to provide a measure of thermomechanical stress in LPBF.

2. Analytical thermal model

Fig. 1(a) shows a schematic of the solution domain for the heat transfer analysis of LPBF. The laser moves in the X and Y directions according to the scanning strategy along a layer and moves up in the Z direction to deposit successive layers. The solution domain including the substrate and the powder bed is assumed to be semi-infinite considering that the substrate size is much larger than the size of the laser beam. The net effect of latent heat of melting and solidification of the alloy on the overall temperature field is considered negligible, which is expected to result in little inaccuracy [15]. The effect of the convective heat transport inside the melt pool is assumed negligible considering the fast cooling of small size melt pools in LPBF. A volumetric heat source term is considered to account for the heat input from the laser beam to the powder particles [15,48]. The specific heat C and thermal conductivity k are considered to be linear functions of temperature (T) as $C = C_0(1 + mT)$ and $k = k_0(1 + mT)$, where m, k_0, C_0 are material parameters. The material properties used in the current work are listed in Table A1 in Appendix A.

The analytical solution for the transient temperature field for LPBF along a single and multiple linear tracks is reported in a previous work [15] and can be expressed as,

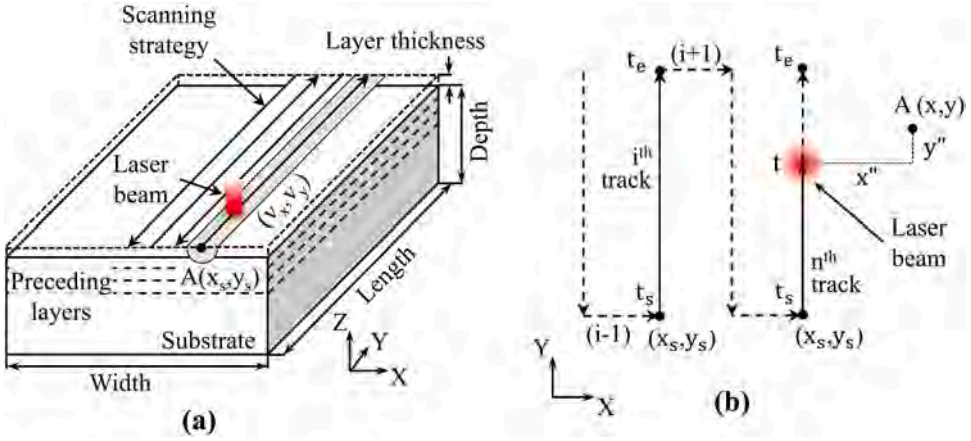

Fig. 1. Schematic presentation of (a) three-dimensional solution domain of laser powder bed fusion showing bidirectional scanning strategy, and (b) nomenclature associated with typical i^{th}, and current (n^{th}) scanning track at time t.

$$T(x,y,z,t) = \frac{1}{m}\left[\left\{\left(U_n(x,\ y,t') + \sum_{i=1}^{(n-1)} U_i(x,\ y,t')\right) + (1+mT_0)^2\right\}^{\frac{1}{2}} - 1\right] \quad (1)$$

where n is the number of scanning tracks traversed by the laser beam till the time instance t and T_0 is the initial temperature of the solution domain. The functional U_n accounts for the effect of heat input to the current scanning track, which is depicted as the n^{th} track, and is expressed as,

$$U_n = P' \int_{t'=t_s}^{t'=t} \frac{1}{\tau_r\sqrt{\tau_h}} \exp\left[-\frac{f_p\{(x")^2+(y")^2\}}{\tau_r} - \frac{f_d(z)^2}{\tau_h}\right] dt' \quad (2)$$

The functional U_i in Eq. (1) accounts for the contribution due to the net heat input during the scanning of each of the previously scanned, i^{th} track, and can expressed as,

$$U_i = P' \int_{t'=t_s}^{t'=t_e} \frac{1}{\tau_r\sqrt{\tau_h}} \exp\left[-\frac{f_p\{(x")^2+(y")^2\}}{\tau_r} - \frac{f_d(z)^2}{\tau_h}\right] dt' \quad (3)$$

In Eq. (2 & 3),

$$P' = \frac{4m\eta P f_p\sqrt{f_d}}{\rho C_0 \pi\sqrt{\pi}} \quad (4)$$

In Eq. (2-4), P is the laser power, η is the absorption coefficient of powder particles, f_p, and f_d are the laser intensity distribution factors in the in-plane (X & Y), and the depth (Z) directions, respectively, and ρ is the density of the alloy [15]. The term τ_r equals to $[4f_p\alpha(t-t') + r_b^2]$ and τ_h equals to $[4f_d\alpha(t-t') + h^2]$, which depict the extent of thermal diffusion in the in-plane (X & Y), and the depth (Z) directions, respectively. Further, r_b is the beam radius, h is the height of the heat source, and α is the thermal diffusivity of the alloy.

The functionals U_n and U_i in Eq. (1) together can account for the planar movement of the laser beam along linear and non-linear tracks for a scanning strategy using two composite variables x" and y". Fig. 1(b) shows a schematic of individual scanning tracks with the arrows indicating the scanning direction. Each scanning track is described in terms of its starting location (x_s,y_s) and the time to cover the track with a scanning speed in terms of the starting time t_s, and the ending time t_e. The variables x" and y" represent the distance between a point of interest (A) and the center of the laser beam at any time t′, and are expressed as,

$$x" = x - g_x(t') \quad (5)$$

$$y" = y - g_y(t') \quad (6)$$

where, g_x and g_y are two functionals, and describe the trajectory of a scanning track.

Fig. 2(a-d) shows schematic views of four commonly used scanning track trajectories in LPBF [49,52,54]. For a scanning strategy comprising of single and multiple linear scanning tracks as shown in Fig. 2(a), the variables x" and y" are expressed as,

$$x" = x - \{x_s + v_x(t'-t_s)\} \quad (7)$$

$$y" = y - \{y_s + v_y(t'-t_s)\} \quad (8)$$

where (x_s,y_s) is the starting location of a scanning track, t_s, is the starting time, and v_x and v_y are the scanning speeds in the X and Y directions, respectively. It is worthwhile to note that, the expressions of variables x" and y" as given in Eqs. (7–8) depict the scanning track trajectory descriptions i.e., $g_x(t')$ and $g_y(t')$ functionals in Eqs. (5–6). Hence, for a linear track, $g_x(t')$ and $g_y(t')$ are simply the parametric equations of a line, calculating X and Y coordinates of the beam location in terms of the starting point of the line, (x_s,y_s), scanning speeds, v_x and v_y, and the travel time (t'-t_s). Likewise, x" and y" terms for curvilinear scanning tracks are obtained by substituting the parametric equations of the corresponding curves expressed as $g_x(t')$ and $g_y(t')$ in Eqs. (5–6).

Considering a circular scanning track with a radius r_c as shown in Fig. 2(b) and the laser beam moving along the track in the anti-clockwise direction at a constant scanning speed of v_c, the variables x" and y" can be expressed as,

$$x" = x - \{x_c + r_c\cos[(v_c/r_c)(t'-t_s)]\} \quad (9)$$

$$y" = y - \{y_c + r_c\sin[(v_c/r_c)(t'-t_s)]\} \quad (10)$$

where (x_c,y_c) is the center of the circular track and (x_c+r_c,y_c) is the starting location. For a spiral-in scanning strategy with the outer radius of the track as r_p as shown in Fig. 2(c) and the laser beam moving inward along the spiral path from a starting location (x_p+r_p,y_p), the variables x" and y" can be written as,

$$x" = x - \left\{x_p + r_p\sqrt{1-(t'-t_s)/S}\cos\left[-2\pi N\sqrt{1-(t'-t_s)/S}\right]\right\} \quad (11)$$

$$y" = y - \left\{y_p + r_p\sqrt{1-(t'-t_s)/S}\sin\left[-2\pi N\sqrt{1-(t'-t_s)/S}\right]\right\} \quad (12)$$

where N is the number of loops in the spiral and S is the time to complete N loops. For the laser beam moving along a circular beam oscillation scanning track of radius of r_o, with an oscillation frequency ν as shown in

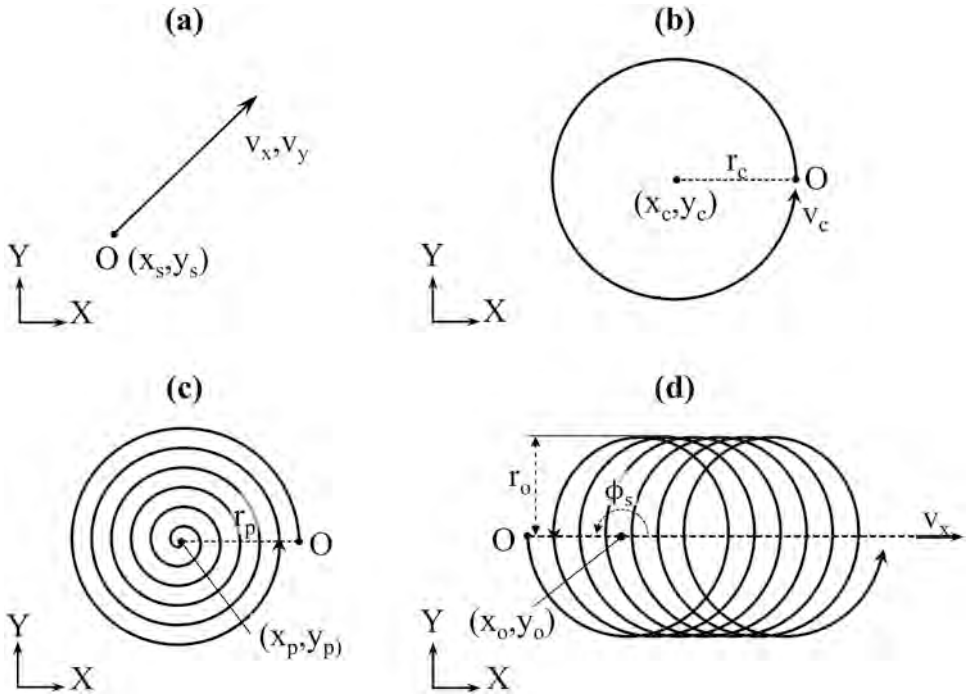

Fig. 2. Schematic representation and nomenclature for (a) linear, (b) circular, (c) spiral-in, and (d) circular beam oscillation scanning strategy. 'O' denotes the starting location of each scanning strategy.

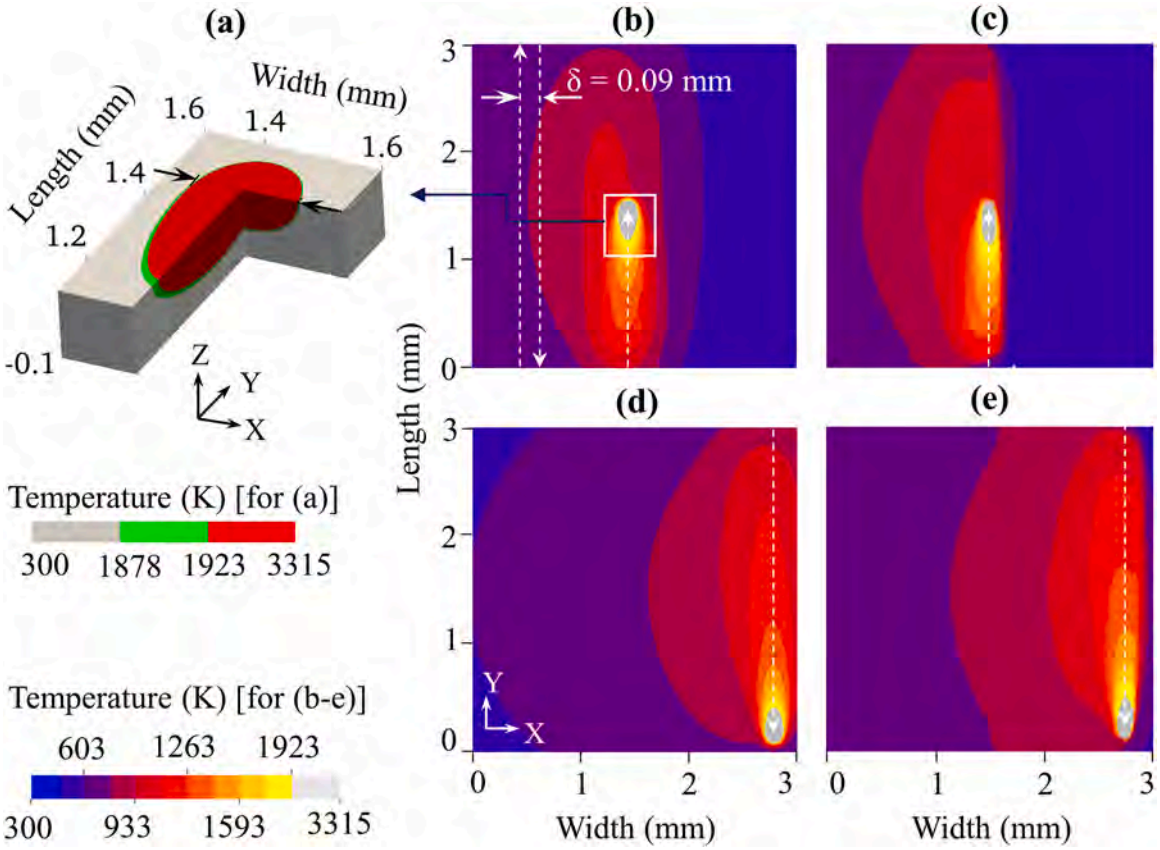

Fig. 3. Computed temperature field for LPBF of Ti6Al4V with a bidirectional scanning for P = 82.5 W, v = 0.5 m/s, and δ = 0.09 mm. (a) Analytically computed 3D view of melt pool at a time instant, t = 0.0875 s; (b) analytically computed, and (c) numerically calculated [11] temperature field along the layer at t = 0.0875 s; (d) analytically computed and (e) numerically calculated [11] temperature field along the layer at t = 0.175 s.

Fig. 2(d), the variables x" and y" can be written as,

$$x" = x - \{x_o + v_x(t' - t_s) + r_o\cos[2\pi\nu(t' - t_s) + \phi_s]\} \quad (13)$$

$$y" = y - \{y_o + r_o\sin[2\pi\nu(t' - t_s) + \phi_s]\} \quad (14)$$

where (x_o, y_o) is the center of the starting circle, ϕ_s is the phase angle corresponding to the starting location of the scanning track on the starting circle, and v_x is the linear speed of the track deposition in the X-direction.

3. Thermal model testing and validation

The analytical model is used first to calculate the temperature field for a bidirectional scanning strategy and the computed results are tested with that reported from a comprehensive numerical model [11]. Secondly, the analytical model is tested rigorously to compute the temperature field for a circular scanning track. The model is used next to compute temperature field and melt track sizes for a spiral-in scanning strategy. The computed melt pool profiles are tested with the corresponding experimentally measured melt track shapes and sizes from the literature [54]. Lastly, the model is used to compute the temperature field for LPBF with a circular beam oscillation scanning strategy, and the accuracy of the computed melt track shapes, dimensions, and cooling rates is tested [52].

3.1. Temperature field for bidirectional scanning strategy

Fig. 3 shows the computed temperature field for LPBF of Ti6Al4V with a bidirectional scanning and for a laser power of 82.5 W, scanning speed of 0.5 m/s and hatch spacing of 0.09 mm [11]. Fig. 3(a) presents the analytically calculated three-dimensional temperature field in the vicinity of the laser beam at a time instant of 0.0875 s, when the laser beam is halfway in the layer. The liquidus temperature isotherm depicts the melt pool boundary and the estimated melt pool width of 0.13 mm agrees well with the corresponding reported numerically computed value of 0.14 mm [11].

Fig. 3(b) shows the analytically computed temperature field on the top surface of the powder bed at 0.0875 s with the high temperature isotherms near the current scanning track. The heated region indicates the already deposited tracks while the un-melted powder region presents a much lower temperature. The analytically computed temperature field in Fig. 3(b) agrees well with that reported by a comprehensive numerical model [11], shown in Fig. 3(c). A little mismatch of the temperature contours in Fig. 3(b) and (c) in the region, which is yet to be scanned, is attributed to the simplified assumption of homogenous materials properties for the powder bed and solidified region. Fig. 3(d)

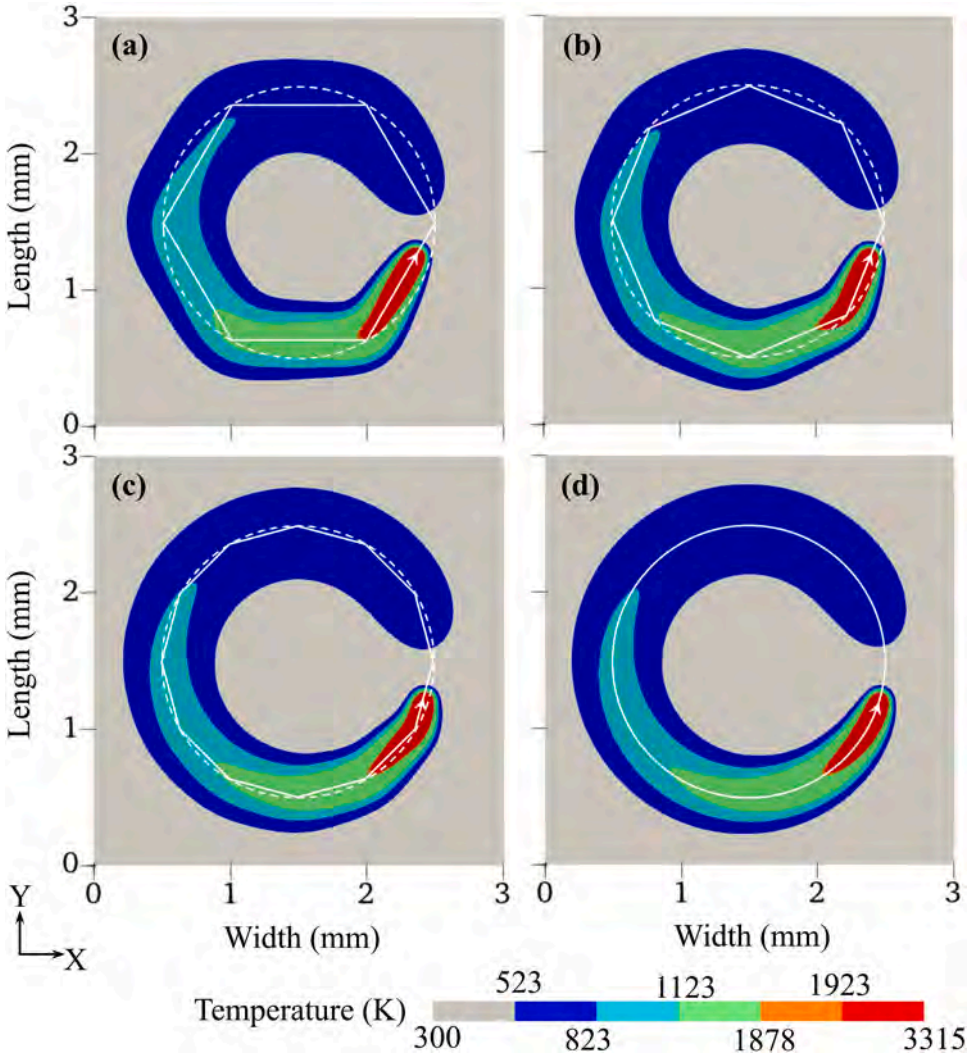

Fig. 4. Analytically calculated temperature field for LPBF of Ti6Al4V with P = 280 W along a circular track of 1 mm radius considering an anti-clockwise rotation of the laser beam. The curvilinear nature of the scanning path is simulated using (a) 6, (b) 8, and (c) 12 linear tracks, and (d) an actual circle to depict the sensitivity of the computed temperature field to the scanned path. The actual scanned path in each case is shown by a solid white line.

and (e) show the analytically calculated and the corresponding numerically computed [11] temperature field at 0.175 s when the laser beam has nearly finished the scanning of the layer. A comparison of Fig. 3(d) and (e) shows a fair agreement between the analytically computed and the corresponding numerically computed temperature contours. Overall, Fig. 3(b-e) show that the analytical model can provide a fair estimate of the transient thermal field for LPBF with multiple linear scanning tracks and bidirectional scanning.

3.2. Temperature field for circular tracks

Scanning along circular tracks is oftentimes required in LPBF to produce parts with complex shapes [49] and to reduce part defects [52, 55]. The circular tracks are commonly modelled as several piecewise linear tracks that reduce the computed accuracy and escalate the computational time [16,17]. The developed analytical model is tested to simulate the temperature field for LPBF of Ti6Al4V along a circular scanning track of radius 1 mm with a laser power of 280 W and scanning speed of 1 m/s. The circular track is simulated as a summation of multiple linear segments and also as a truly circular one following Eqs. (7–8) and Eqs. (9–10), respectively.

Fig. 4(a-c) show the computed temperature field at 6 ms for the circular track linearized as six, eight, and twelve segments, respectively. In contrast, Fig. 4(d) shows the computed temperature field at the same time instant of 6 ms when a perfect circular track is considered for the analytical model calculation. A comparison of Fig. 4(a-c) shows that the melt pools follow a polygonal trajectory as the circular track is approximated by multiple linear tracks. The scanning path becomes closer to a true circular track with a reducing effect of the linearization as more linear segments are used as shown in Fig. 4(a-d). Multiple short linear segments can better represent a true circular track length and the computed temperature field but augment volume of calculations [16,17, 56]. In contrast, the ability to simulate an exact circular and curvilinear track yields a more accurate temperature field and reduces the overall volume of calculations. A comparison of Fig. 4(a-c) and Fig. 4(d) shows an overestimation of the melt pool by 15–25% when the circular track is simulated by multiple linear tracks especially for longer segments and near to the junction between two segments.

3.3. Temperature field for spiral-in scanning track

LPBF using a spiral-in scanning strategy has shown potential to provide a uniform temperature distribution, consistent width, and reduced thermal distortion along the deposited tracks [22,43,54,57]. However, scanning near the center of spiral path can cause heat accumulation that may lead to excess melt deposit and deteriorate the surface quality of the LPBF part [54,58]. A study is therefore required to understand the influence of spiral-in scanning strategy on the resulting shape and size of the melt tracks. Fig. 5(a) shows the analytically computed melt track for LPBF of SS 17–4 along a spiral-in path corresponding to a reported experimental investigation [54]. The spiral-in scanning path is modeled analytically following Eqs. (11–12). Fig. 5(a) shows the analytically computed melt track along the spiral path. The computed melt track is thinner at three locations, shown by arrows, which is due to a reduced laser power from 100 W to 60 W for a duration of 300 μs at each location [54]. In contrast, the computed melt track

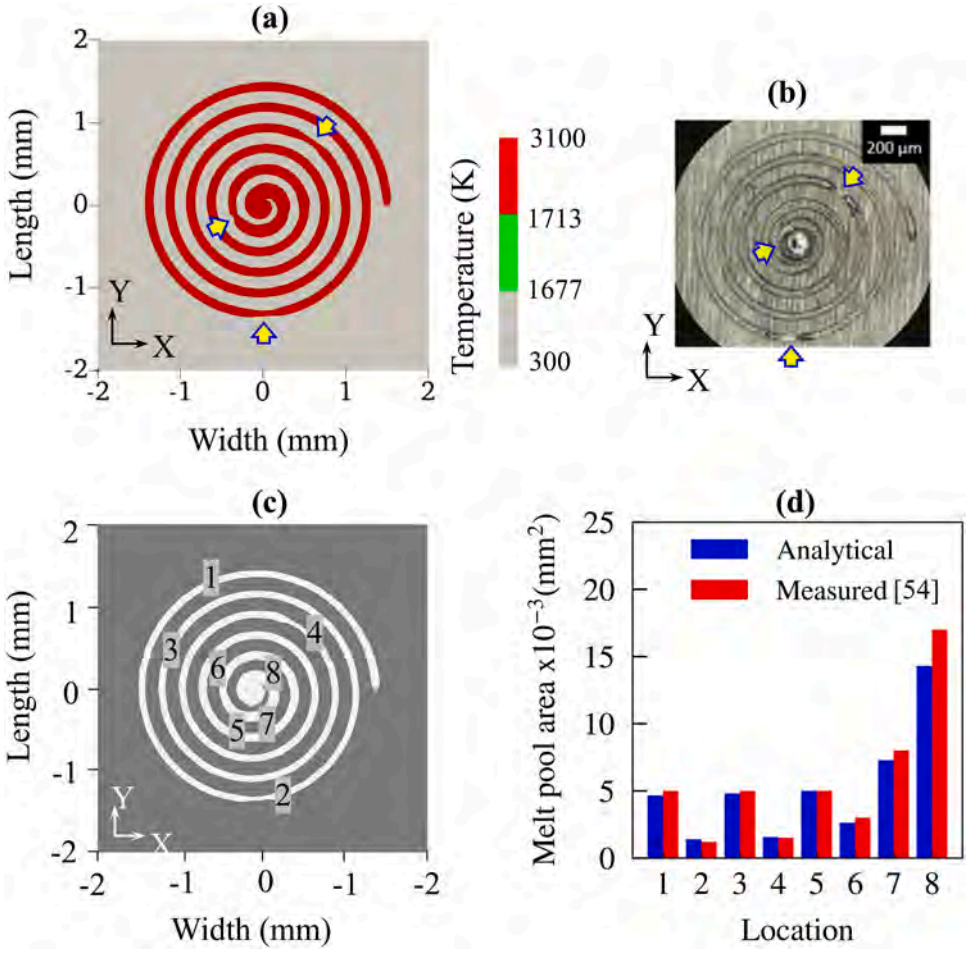

Fig. 5. Spiral-in scanning during LPBF of SS 17-4, (a) analytically estimated melt track profile, (b) experimentally observed deposit geometry, (c) locations 1–8 on the deposit track (for melt pool area comparison), (d) analytically estimated and experimentally measured [54] melt pool areas.

increases towards the inner loops of the spiral as the heat input per unit length increases for shorter spiral size and lower scanning speed [54]. The corresponding measured spiral track in Fig. 5(b) [54] also shows thinner or broken deposits at three locations and a large deposit at the center. Overall, Fig. 5(a-b) represent a fair agreement between the analytically computed and the corresponding experimentally measured spiral track shapes.

The analytical model is next used to compute the melt pool shapes at eight locations, as shown in Fig. 5(c). A comparison of the computed and the corresponding experimentally measured [54] melt pool areas at those locations is shown in Fig. 5(d), which presents a fair agreement with the range of discrepancy from 5% to 15%. The melt pool areas at 1, 3, and 5 are larger as they correspond to the track locations deposited with a higher laser power of 100 W. The melt pool area increases further at locations 7 and 8 due to gradually reduced scanning speed and resulting greater rate of heat input while depositing the inner loops of the spiral track. In contrast, the melt pool areas at locations 2, 4, and 6 are smaller due to the reduced laser power [54] from 100 W to 60 W for scanning of the corresponding regions of the track.

3.4. Temperature field for circular beam oscillation scanning strategy

In the circular beam oscillation scanning strategy, a laser beam is oscillated in a circular trajectory as the beam moves linearly along the desired scanning path [52]. The circular beam oscillation scanning strategy in LPBF could reduce the micropores and cracks [52,59], lower the thermal stresses [55], and improve the ductility of the final part [55, 60]. However, the influence of laser power, scanning speed, oscillating circle radius, and oscillation frequency on temperature field and melting pattern is not well understood [61]. The use of beam oscillation techniques for LPBF is still emerging and related thermal analysis is rarely reported in the literature [55,60]. The developed analytical model is therefore employed to compute the temperature field, melt track shape, and thermal cycles in LPBF with a circular beam oscillation scanning strategy. The schematic of the circular beam oscillation scanning strategy is shown in Fig. 2(d), and the path is considered following Eqs. (13–14).

3.4.1. Melt pool evolution

Fig. 6(a) shows the analytically computed temperature field at a time instant of 0.01 s for LPBF of IN718 with 300 W laser power and a circular beam oscillation scanning path with 0.5 mm oscillating circle radius (r_o), 100 Hz oscillation frequency (ν), and 0.01 m/s linear speed in X direction [52]. Fig. 6(a) depicts the melt pool and the heated region along the circular path traversed by the laser beam in the first oscillating circle. The laser advances in the X direction and Fig. 6(b) shows the temperature field at the end of the fifth consecutive circular track. The melt pool size increases in the radial direction and along the circumference of the oscillating circle due to preheating during the deposition of previous tracks. Fig. 6(c) shows the temperature field at the end of the tenth circle and indicates an overlapping of the melt pools along the adjacent tracks resulting in a near circular shaped pool as shown by the red colored region.

Fig. 6(d) shows the analytically computed temperature field during scanning along the twenty-first circle with the boundary of the deposited and solidified track shown with a dotted line. A comparison of the analytically calculated melt pool shape and the solidified track in Fig. 6 (d), and the corresponding experimentally measured solidified track in Fig. 6(e) [52] shows a fair agreement. For example, the estimated width of the solidified track is around 1.4 mm in Fig. 6(d) in comparison to the experimentally measured track width of around 1.35 mm [52].

3.4.2. Effect of oscillating circle radius on temperature field

The melt pool shape and size, and the deposited track width are influenced by the radius (r_o) of the oscillating circle for a circular beam oscillation scanning strategy [52]. The analytical model is used to

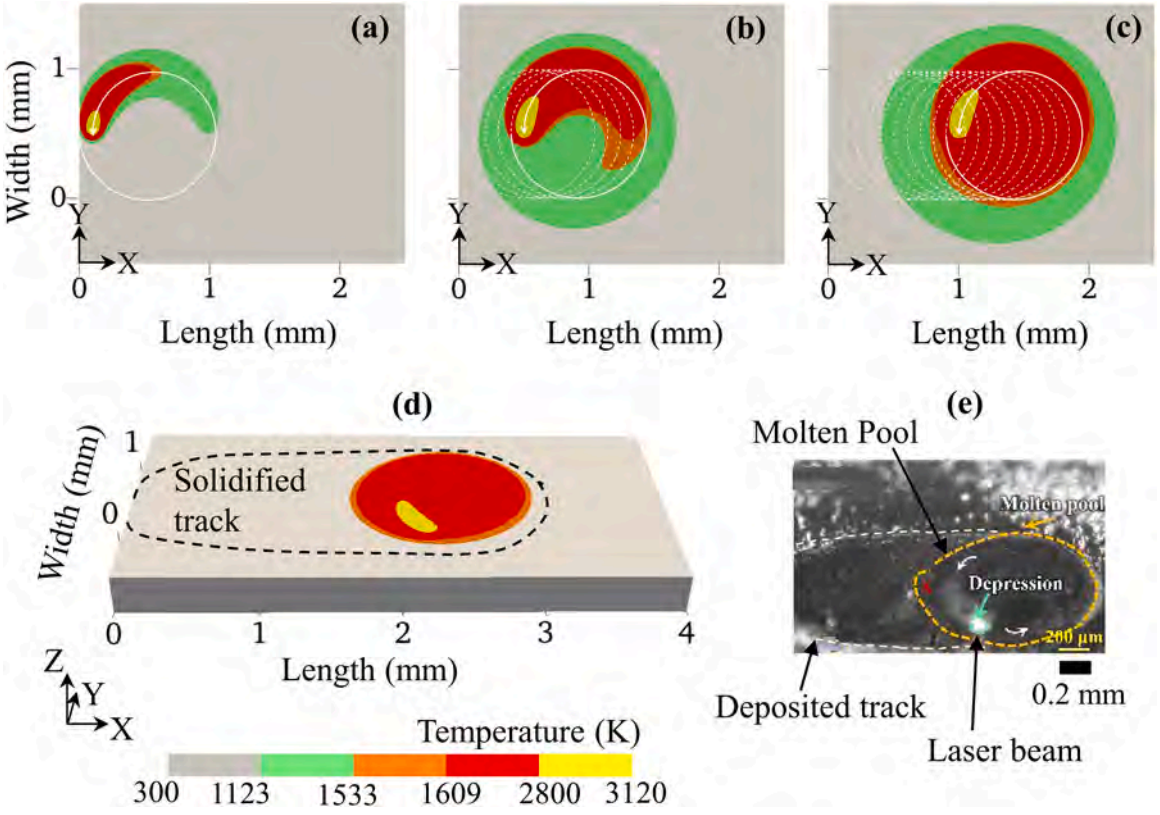

Fig. 6. Analytically computed temperature field in circular beam oscillation scanning strategy (laser path shown with white lines), for LPBF of IN718, using laser power of 300 W, and r_o of 0.5 mm, at (a) 0.01 s, (b) 0.05 s, (c) 0.10 s, & (d) 0.201 s, and (e) melt pool image of the corresponding experiment [52].

simulate LPBF of IN718 with the oscillating circle radii (r_o) of 1.1 mm, 0.8 mm, and 0.5 mm. The corresponding beam oscillation scanning strategies are referred to as S1, S2, and S3, respectively. Fig. 7(a) shows the laser path in S1 with the region ABCDEF encompassing the 31st to 35th circular scanning tracks. The corresponding temperature field is shown in Fig. 7(b) depicting the melt pools and the heated regions for five adjacent circular tracks. Fig. 7(b) shows that the melt pools spread along the circumference of the circular tracks. The consecutive melt pools of nearly equal depth indicate a fairly stabilized temperature field at the end of the 35th track. It is noteworthy that the analytical model can quickly simulate several scanning tracks, while the use of numerical models for the same is likely to remain infeasible due to the associated computational time and resource demands.

Fig. 7(c-d) shows the laser path and the corresponding computed temperature field for the scanning strategy S2. A comparison of Fig. 7(b) and Fig. 7(d) shows the melt pools and heated region for S2 agree well with the circular track, which is attributed to the reduced oscillating circle radius (r_o) from 1.1 mm to 0.8 mm. Further, the melt pools for the S2 strategy are deeper than those for S1, which is attributed to increased heat input due to the smaller radius of the oscillating circle. Fig. 7(e-f) shows the laser path and the corresponding computed temperature field for the scanning strategy S3 with a smaller oscillating circle radius of 0.5 mm. Fig. 7(f) shows larger and deeper melt pools than that for both S1 and S2 scanning tracks, and a greater influence of preheating due to laser traversing along smaller size oscillating circles for S3 scanning track.

Overall, Fig. 7 shows that the deposited track width corresponds to the oscillating circle radius for a related scanning strategy. Larger oscillating circles result in smaller melt pools with lesser interference between the adjacent pools and tend to form ring shaped solidification tracks. In contrast, smaller oscillating circles lead to large circular melt pools due to the merging of pools along adjacent circular tracks. The melt pool depth with smaller oscillating circles increases as the heating occurs in smaller circles with a reduced scanning speed and a constant oscillation frequency. The effect of the oscillating frequency on the melt pool width and depth of the deposited tracks is studied next.

3.4.3. Melt track shape and dimensions

Fig. 8(a-d) shows a comparison of the transverse cross-sections of the computed melt tracks and the corresponding experimentally measured tracks [52] for LPBF of IN718 with a constant oscillation frequency (ν) and two oscillating circle radii (r_o).

Fig. 8(a-b) shows that the analytically calculated melt track and the actual deposited track assume a rectangular shape with a fairly high width to depth ratio for a larger oscillating circle radius (r_o) of 0.8 mm. As the oscillating circle radius (r_o) is reduced from 0.8 mm to 0.5 mm, the heat input concentrates in smaller regions resulting in deeper melt pools and tracks, as shown in Fig. 8(c-d). In contrast, an increase in oscillation frequency (ν) from 100 Hz to 300 Hz for the oscillating circle radius (r_o) of 0.5 mm results in shallower melt pools and deposited tracks, as shown in Fig. 8(e-f). This is attributed to a faster scanning speed for a greater oscillation frequency (ν) and consequently reduced

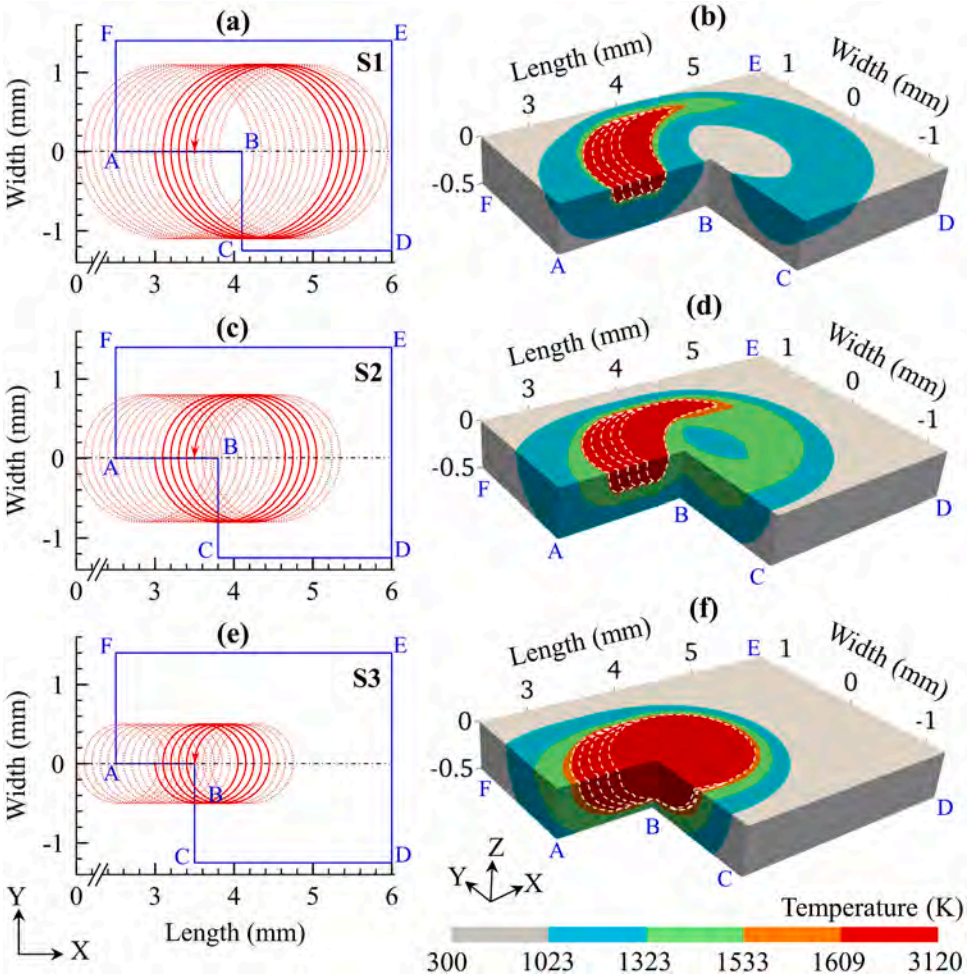

Fig. 7. Circular beam oscillation scanning strategy for LPBF of IN718, using laser power of 300 W, oscillation frequency of 100 Hz, and radius of oscillating circle, r_o of (a) 1.1 mm, (c) 0.8 mm, (e) 0.5 mm, and temperature field at the completion of each of the 31st to 35th circular scanning tracks with r_o of (b) 1.1 mm, (d) 0.8 mm, (f) 0.5 mm.

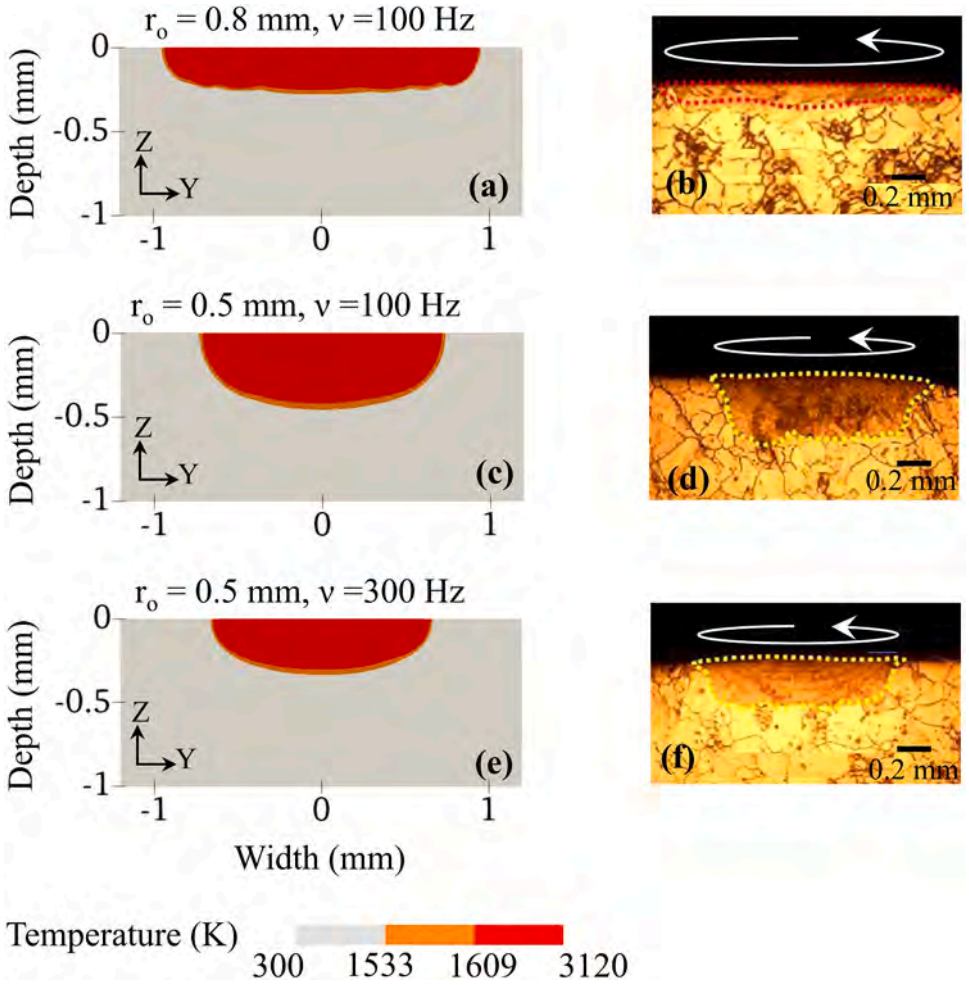

Fig. 8. Analytically computed melting tracks for circular beam oscillation scanning strategy in LPBF of IN718, with P = 300 W and (a) r_o = 0.8 mm, ν = 100 Hz, (c) r_o = 0.5 mm, ν = 100 Hz, and (e) r_o = 0.5 mm, ν = 300 Hz, and corresponding experimentally observed [52] cross-sections of deposited tracks, (b) r_o = 0.8 mm, ν = 100 Hz, (d) r_o = 0.5 mm, ν = 100 Hz, and (f) r_o = 0.5 mm, ν = 300 Hz. White arrows indicate directions of laser beam oscillations.

heat input. The analytically calculated melt track profiles agree well with the corresponding measured track dimensions with a range of discrepancy from 5% to 15%. Overall, Fig. 8 shows that smaller oscillating circles and frequency increase the melt track depth. A smaller oscillating circle radius also reduces melt track width, but the oscillating frequency has shown little effect on the melt track width for the range of conditions examined in the present work.

3.4.4. *Thermal cycle and estimation of PDAS*

The computed temperature field is used to calculate the important

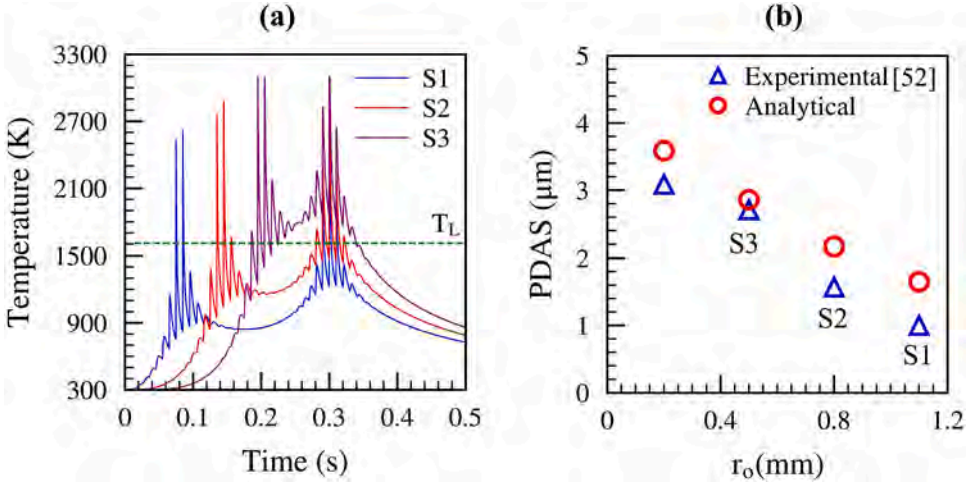

Fig. 9. (a) Computed thermal cycles at a point on the surface at 3 mm from the starting point of the circular beam oscillation scanning strategy for S1, S2 and S3. (b) Primary dendrite arm spacing (PDAS) is estimated using computed cooling rates and the corresponding experimentally measured values [52].

metallurgical variables such as the thermal cycle, the solidification cooling rate, and the primary dendrite arm spacing (PDAS) for LPBF of IN718 with the beam oscillation scanning path S1, S2, and S3, as defined in section-3.4.2. A point 'M' is selected along the centerline of the circular beam oscillation scanning path at a distance of 3 mm from the starting point of the first oscillating circle as illustrated in Appendix B. Fig. 9(a) shows the computed thermal cycles at point 'M' for the S1, S2 and S3 scanning paths. A comparison of the computed thermal cycles for S1 and S2 scanning paths shows repeated melting and freezing at the monitoring point 'M'. In contrast, the monitoring point 'M' remains molten for a longer duration for S3 scanning path, which is attributed to the shorter oscillating circular scanning track. The slower solidification for the S3 scanning path has eventually resulted in reduced porosity [55,62].

Fig. 9(b) shows the analytically estimated and the corresponding experimentally measured primary dendrite arm spacing (PDAS) [52] as a function of the radius r_o of circular tracks. The PDAS for IN718 alloy is estimated as a function of the solidification cooling rate, $\dot{T}$ as PDAS $= 80(\dot{T})^{-0.33}$ [63]. The computed solidification cooling rates for the circular beam oscillation scanning are found to be lower than those for linear scanning tracks [64]. For example, the computed solidification cooling rate $\dot{T}$ for the oscillating circular track of radius (r_o) 0.2 mm is around 1.22×10^4 K/s in comparison to 5.0×10^6 K/s, reported for a typical linear track [64]. The resulting range of values of PDAS for the oscillating circular tracks is around 3.5–1.5 μm in comparison to 1.1–1.0 μm for typical linear tracks [64]. Fig. 9(b) confirms further that the PDAS reduces with an increase in the circular track radius (r_o), which is attributed to higher cooling rate $\dot{T}$ with greater track radii r_o.

Overall, Fig. (6-9) show that the analytical model can provide a fairly accurate estimation of the temperature field for LPBF with a circular beam oscillation scanning strategy. The computed temperature field can be used further to derive the thermal cycle, solidification cooling rate, and PDAS, which are important metallurgical variables to assist a prior estimate of build structure and property.

3.5. Computational time

The aforementioned discussions show that the analytical model can provide a fairly substantive temperature field, melt pool sizes, and thermal cycles for LPBF with diverse scanning strategies. The computational efficiency of the analytical model is another important aspect [17]. Table 1 presents a comparison of the computational time to simulate the LPBF of a 10 mm × 10 mm × 0.5 mm build with the circular beam oscillation scanning strategy using the analytical model and reported numerical models [65,66]. The analytical model calculations are performed using an 11th generation core i5 notebook computer with 8 GB RAM. The computational time for the numerical models is estimated based on documented literature. Table 1 shows that the analytical model can simulate curved scanning tracks much faster than corresponding linearized scanning tracks for the same path. Furthermore, the estimated computational times for the reported numerical models to simulate a volume of 50 mm^3 are by far remarkably higher in comparison to that required for the analytical model calculations. This exhibits the strength of the proposed model as a substantive tool for a quick estimation of temperature field for LPBF with varying scanning strategies and of common alloys. A further practical utility of the computed temperature field to obtain a measure of susceptibility to thermal stress is demonstrated next.

Table 1
Comparison of computational time with analytical and reported numerical models for LPBF of a 10 mm × 10 mm × 0.5 mm sample build with circular beam oscillation scanning strategy.

Types of model	Computational time
Analytical heat conduction model with curved scanning tracks	589 s
Analytical heat conduction model with linearized scanning tracks for curved paths [15]	1826 s
FEM based heat conduction model* [65]	~ 169 hrs
Heat transfer and fluid flow model* [66]	~ 248 hrs

* Estimated based on reported simulation time and track length, assuming no further mesh/algorithm optimization and hardware enhancement.

4. Susceptibility of scanning strategy to thermal stress

A suitable scanning strategy to reduce the evolution of thermal stress and distortion is in demand to design an LPBF schedule [1,67]. The susceptibility of a scanning strategy to thermal stress can be evaluated in terms of a temperature non-uniformity (ΔT) metric [43,67] as,

$$\Delta T = \sum_{j=1}^{n_l} \sqrt{\left[\frac{(T_j - T_a)}{n_l T_a}\right]^2} \tag{15}$$

where, n_l, is the number of points selected in the layer, T_j is the calculated temperature at any point j at any time t, and T_a is the average layer temperature at time t. The temperature non-uniformity (ΔT) metric in Eq. (15) is the sum of the normalized deviations between the temperature at different points across the layer and the instantaneous average layer temperature. The temperature non-uniformity (ΔT) metric is calculated for the entire laser traverse along the given scanning path for a layer and compared across scanning strategies to estimate their susceptibility to thermal stress. The temperature non-uniformity (ΔT) metric provides a measure of the overall temperature gradient and a resulting thermal stress for LPBF of a powder alloy.

4.1. Effect of scanning track length

The analytical model is first used to investigate the effect of scanning track length (L_S) for LPBF of Ti6Al4V with a laser power of 200 W, scanning speed of 1 m/s, and hatch spacing of 0.1 mm [27]. Fig. 10(a) shows four unidirectional scanning strategies with different track lengths (L_S) for the deposition of a layer of 20 mm×20 mm. Fig. 10(b) shows that the analytically calculated average layer temperature (T_a) increases with time for all the four scanning strategies.

Fig. 10(c) shows a rapid increase of the temperature non-uniformity (ΔT) metric for the longer scanning track length (L_S) of 20 mm, which is attributed to the rapid cooling of the solidified track as the laser moves away. The temperature non-uniformity (ΔT) metric reduces steadily with a reduction in the scanning track length, which is attributed to an increase in the average layer temperature (T_a) with a shorter scanning track. The fluctuating nature of ΔT for shorter scanning tracks is attributed to the multiple rows of shorter scanning tracks (L_S) of 10 mm, 5 mm, and 2.5 mm, as shown in Fig. 10(a).

The maximum temperature non-uniformity (ΔT) metric is construed to cast an indirect measure of the maximum thermal stress [43,44]. Fig. 10(d) presents a comparison of the maximum ΔT for the four scanning strategies that indicates the longer scanning tracks yielding greater thermal stress, which is also confirmed by the reported experimental measurements in literature [27].

4.2. Choice of scanning strategy

The selection of a suitable scanning strategy to reduce thermal stresses is important in LPBF [1,3]. The developed analytical model is used further to assess the susceptibility of four commonly used LPBF scanning strategies [3] to thermal stress in terms of their corresponding temperature non-uniformity (ΔT) metrics. Fig. 11(a) shows four commonly used scanning strategies to deposit a layer of 20 mm×20 mm for LPBF of Ti6Al4V with a laser power of 200 W, scanning speed of

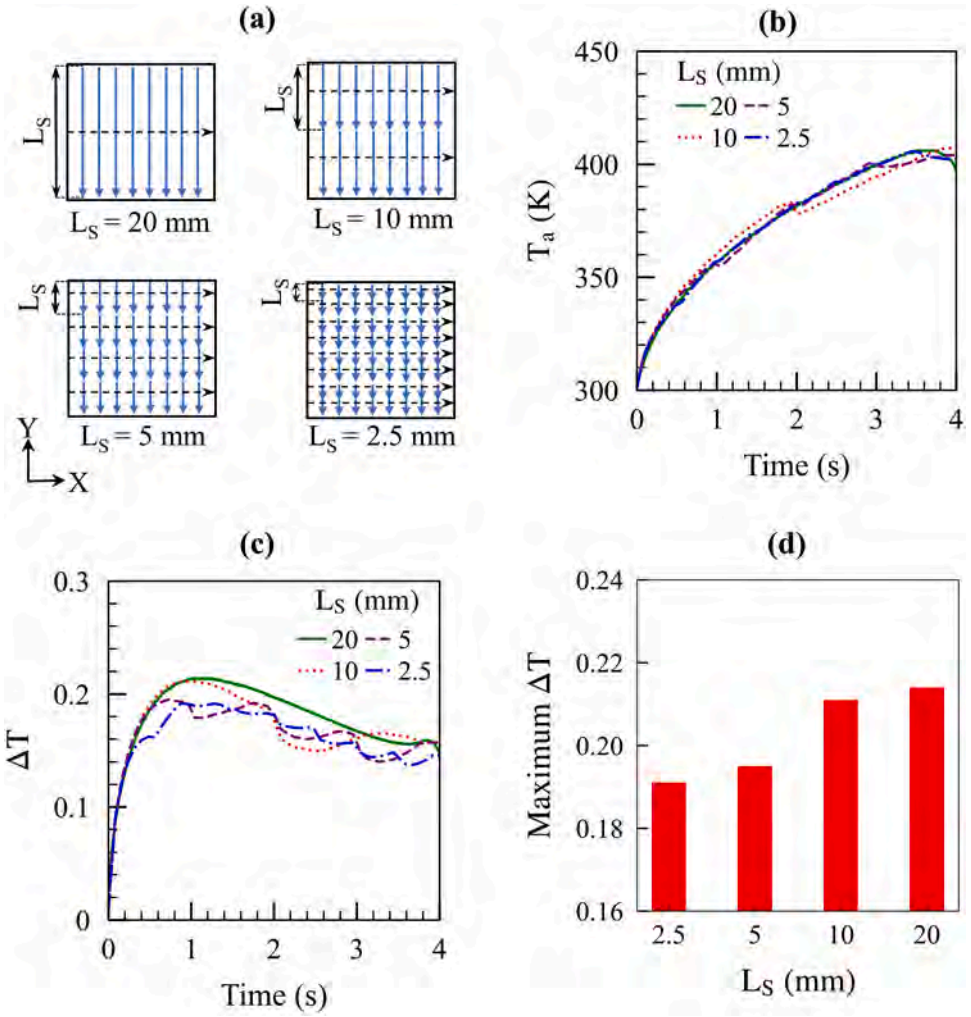

Fig. 10. (a) Schematic of scanning strategies with scanning track length in LPBF of Ti6AL4V, with laser power of 200 W, scanning speed of 1 m/s, and hatch spacing of 0.1 mm [27], (b) average layer temperature (T_a), (c) temperature non-uniformity (ΔT), and (d) maximum temperature non-uniformity (ΔT).

1 m/s, and hatch spacing of 0.1 mm. Fig. 11(b) shows that the analytically computed average layer temperature (T_a) gradually increases as the scanning progresses except for the in-out strategy, where the average layer temperature (T_a) reduces slightly towards the completion of the outer layers.

Fig. 11(c) shows that the variation of the temperature non-uniformity (ΔT) metric is similar for unidirectional and bidirectional strategies indicating a negligible overall effect for the reversal of scanning direction in alternating tracks for the bidirectional strategy. For the in-out strategy, local heating starts along short tracks at the center of the layer resulting in rapidly increasing ΔT that reduces as the scanning continues to the outer and wider tracks. In contrast, ΔT is low in the beginning for the out-in strategy, which increases as the scanning moves into the shorter tracks towards the center of the layer. For both in-out and out-in strategies, a localized accumulation of high heat and resulting stress as the beam scans over shorter tracks is therefore anticipated from the corresponding trend of ΔT, which, in principle, is in line with the observation by Cheng et al. [45]. A relatively smaller value of the maximum ΔT in Fig. 11(d) for the out-in strategy in comparison to that for the other strategies considered in the present work is attributed to the preheating of the inner region as the beam moves from the outer towards the inner tracks. A recent investigation by Jia et al. [68] has also reported a smaller stress for an out-in strategy in comparison to in-out and bidirectional strategies, and several other studies have also opined for smaller distortion [22,43,69] and stress [43,69] for out-in strategy.

4.3. *Influence of island scanning strategy*

In *island* scanning strategy the total layer area is divided into several small subareas, referred to as *islands*, which are scanned in a certain sequence to reduce the resultant thermal stress and distortion [5,29]. The developed analytical model is used further to assess the influence of *island* scanning strategies in LPBF.

Fig. 12(a) shows four scanning strategies considered to deposit a layer of 20 mm×20 mm for LPBF of H13 with a laser power of 180 W, scanning speed of 0.6 m/s, and hatch spacing of 0.1 mm [29]. First a bidirectional scanning strategy with scanning track length of 20 mm is analyzed for LPBF deposition of the layer. The layer is divided into 4 mm×4 mm sized *islands* and three scanning strategies according to the sequence of scanning the islands is shown in Fig. 12(a). For *successive* scanning strategy, *islands* are scanned directly one after the other. For the *least heat influence* (*LHI*) *chessboard* scanning strategy, each subsequent *island* is chosen such that it lies as far as possible from the current *island* [29,38]. Finally, the *random chessboard CL* scanning strategy involves a randomized scanning sequence, and it is often used in commercial LPBF machines [29,70]. For three *island* strategies, each individual *island* is scanned with a bidirectional scanning strategy of 4 mm scanning tracks and the direction of scanning is rotated by 90^0 for each adjacent *island*, as shown schematically in Fig. 12(b).

Fig. 12(c) shows that the overall temperature non-uniformity (ΔT) metric for *island* scanning strategies is lower than that for the

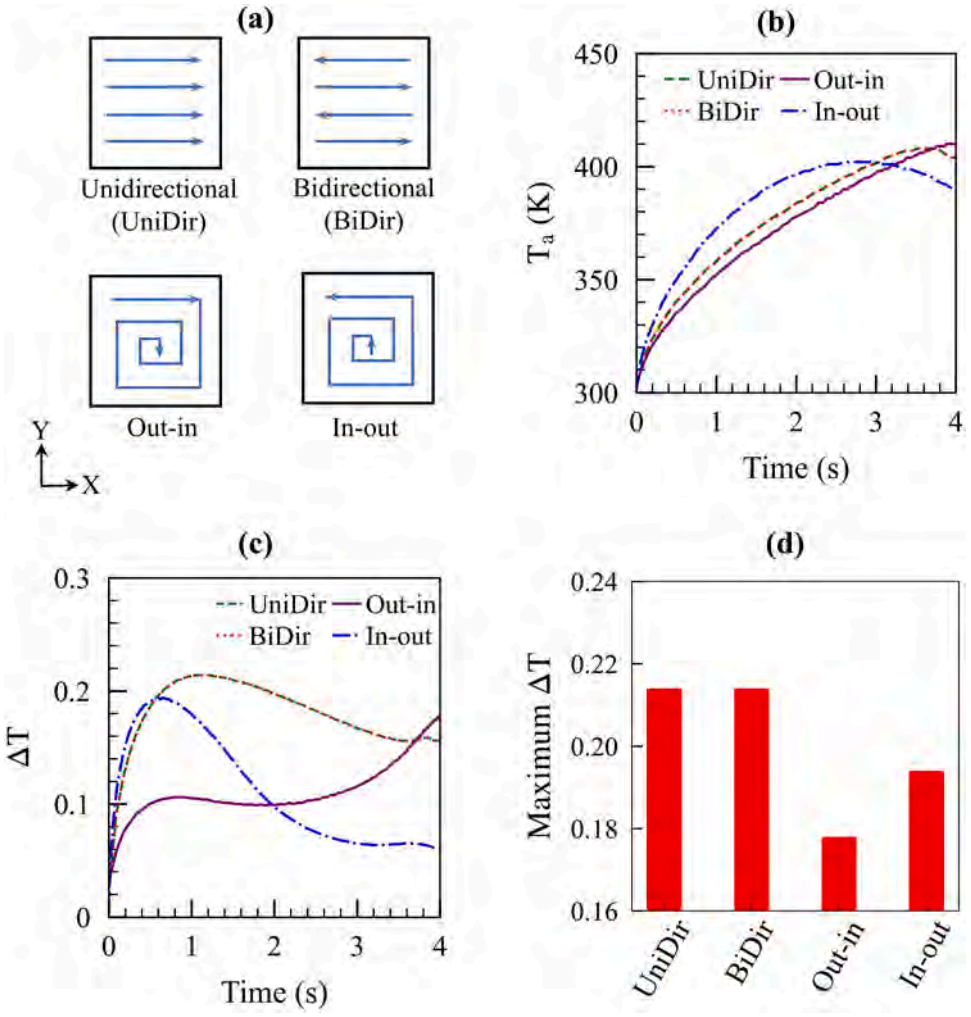

Fig. 11. (a) Schematic of four scanning strategies in LPBF of Ti6AL4V, with laser power of 200 W, scanning speed of 1 m/s and hatch spacing of 0.1 mm, (b) average layer temperature (T_a), (c) temperature non-uniformity (ΔT), and (d) maximum temperature non-uniformity (ΔT).

bidirectional scanning strategy indicating the effect of scanning along shorter tracks. The overall magnitudes of ΔT for bidirectional and *successive* scanning strategies are comparable, as in both cases the scanning occurs from one end of the layer to the other resulting in similar heating and cooling behavior across the layer. For *LHI chessboard* and *random chessboard CL*, the *islands* are scanned in a spread manner in the sequences as shown in Fig. 12(a) yielding an even temperature distribution and lower ΔT. Fig. 12(d) shows lower values of the maximum ΔT for all *island* scanning strategies in comparison to that for the bidirectional scanning strategy. Both the *LHI chessboard* and *random chessboard CL* show lower values of the maximum ΔT and are likely to result in smaller thermal stresses as also reported in literature [29].

Figs. (10–12) show that a novel temperature non-uniformity metric (ΔT), estimated using the analytically computed temperature field, can provide a quick measure of the effect of scanning strategies on the evolving thermal stress in part scale LPBF. The use of similar variables to get a back-of-the-envelope estimate of thermal strain has also been reported in literature [67,71,72]. For example, the propensity of thermal distortion in additive manufacturing (AM) was envisaged by a thermal strain parameter (ε^*) as [71],

$$\varepsilon^* = \frac{\beta \Delta T^*}{EI} \frac{t^*}{F\sqrt{\rho}} H^{3/2} \tag{16}$$

where β is the volumetric thermal expansion coefficient of alloy, (ΔT^*) is the difference between peak temperature and surrounding temperature, EI is the flexural rigidity of substrate, F is the Fourier number, t^* is the deposition time, ρ is the density of alloy and H is the heat input per unit length. Eq. (16) shows that an increase in the temperature gradient (ΔT^*) results in higher value of the thermal strain parameter (ε^*) and is likely to cause greater thermal distortion. For a given LPBF conditions, the proposed temperature non-uniformity metric (ΔT) can be conceptualized as a depiction of (ΔT^*) in Eq. (16). In other words, an increase in the calculated temperature non-uniformity metric (ΔT), proposed in this work, can also be considered as an indirect measure of increasing thermal strain and resulting distortion without much loss of generality. Although more rigorous validations of the proposed temperature non-uniformity metric (ΔT) is warranted to use it as a true estimator or thermal distortion in part scale LPBF, the parameter (ΔT), powered by a fast analytical heat transfer analysis, can certainly serve as a substantive tool to help design of LPBF process.

The aforementioned sections have illustrated that the developed analytical model can compute a reasonably accurate temperature field in LPBF with different scanning strategies at a notably small computational time. A rigorous validation carried out for scanning strategies including linear and curved laser paths showed that the computed transient temperature field and estimated melt pool shapes, thermal cycles, and cooling rates match well with the corresponding results from the literature. Overall, the model provides a quick assessment of the influence of the LPBF scanning strategy on the resulting temperature field, track dimensions, PDAS, and susceptibility to thermal stress

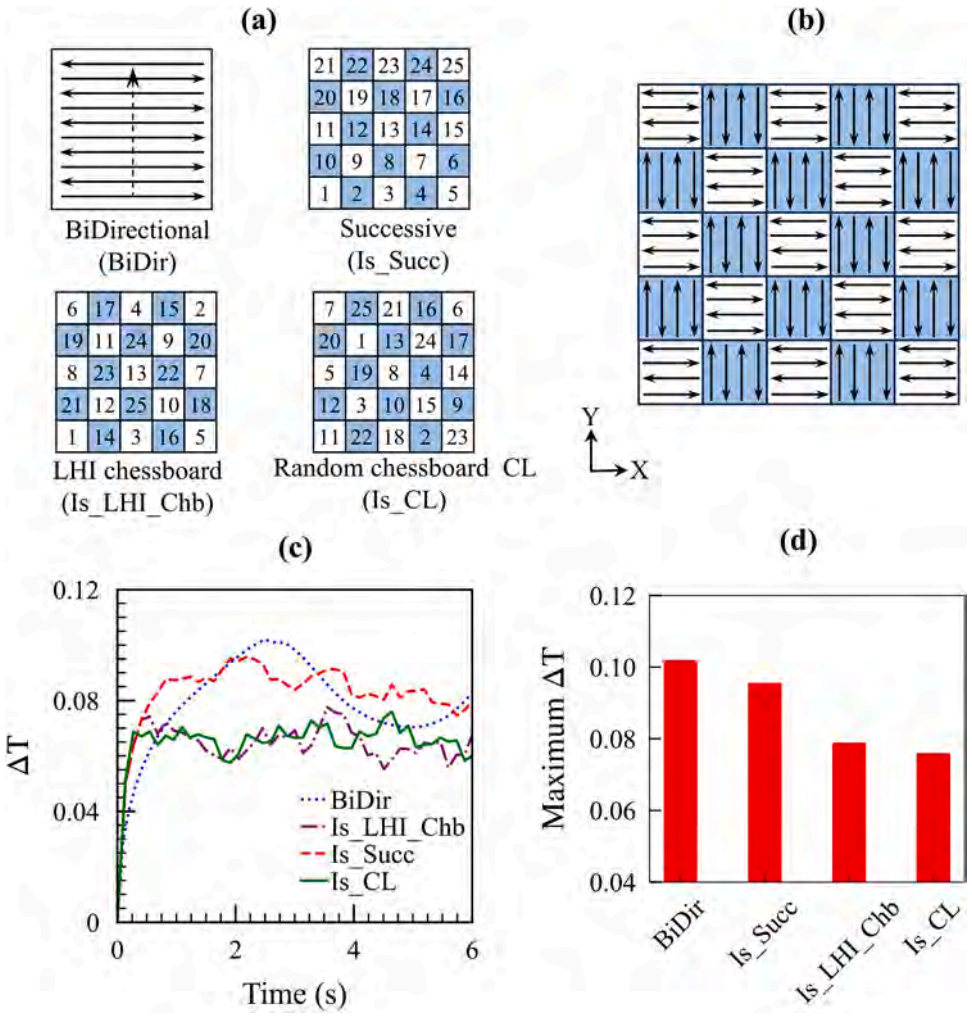

Fig. 12. (a) Schematic of bidirectional scanning strategy and the sequence of scanning *islands* in three *island* scanning strategies for LPBF of H13 [29], (b) direction of scanning tracks for individual *islands*, (c) temperature non-uniformity (ΔT), and (d) maximum temperature non-uniformity (ΔT).

formation, which will help in selecting the optimal scanning strategy. However, the influence of fluid flow in melt pool [73] and recoil pressure [74] is neglected while obtaining a tractable analytical solution. This simplification may pose limits on application of the model to examine the keyhole dynamics [53] and in-depth microstructural investigations [75]. Likewise, the assumption of the semi-infinite solution domain may cause practical challenges in simulating the temperature field near the part boundaries and in the parts with long overhanging regions and lattice structure. Furthermore, though the presented model is significantly faster than existing topical models, its utility for simulating full temperature profiles across large industrial scale part of size in several cm^3 may require enhanced computing resources.

5. Summary and conclusions

An analytical heat transfer model is specifically designed and tested to analyze the thermal effects of various scanning strategies in LPBF. Notably, our focus extends beyond conventional linear paths including circular and widely used various curved scanning paths. The practical utility of the proposed model is demonstrated by examining the effects of the scanning strategy on the formation of thermal stresses during LPBF. Computed temperature field, melt pool shape and dimensions, and cooling rates are compared with corresponding independently measured values for LPBF with bidirectional, spiral, and circular beam oscillation scanning strategies. The computational efficiency of the proposed model is compared with available numerical models. The following are the main conclusions.

- The proposed analytical model could predict a fairly accurate temperature field for LPBF with linear, bidirectional, circular, and spiral scanning strategies.
- For LPBF with circular beam oscillation scanning strategy, the computed melt track dimensions, cooling rates, and the primary dendritic arm spacing are found to be in good agreement with the corresponding independent experimental results. The computed results showed further that the melt track width increased with an increase in the oscillating circle radius, and the track depth increased with the reduction of the oscillating circle radius and oscillation frequency.
- The analytical model can simulate LPBF along a true curvilinear path significantly faster in comparison to mimicking the curved path by multiple linear segments. Overall, the analytical model can provide the computed temperature field along several tens and hundreds of tracks many times faster even when deployed on a notebook computer than available numerical models.
- The calculated temperature non-uniformity across a layer increased with increasing scanning track length, and the maximum temperature non-uniformity could indicate susceptibility to thermal stress. The comparison of four common LPBF scanning strategies showed that the out-in scanning strategy is likely to result in minimal thermal stresses. Among the *island* scanning strategies considered here, the *least heat influence chessboard* and *random chessboard CL* scanning

strategies are likely to be less susceptible to thermomechanical stresses.

CRediT authorship contribution statement

Zagade Pramod R.: Writing – original draft, Methodology, Formal analysis, Data curation, Conceptualization. **De Amitava:** Writing – review & editing, Supervision, Formal analysis, Conceptualization. **Deb-Roy Tarasankar:** Writing – review & editing, Formal analysis, Conceptualization. **Gautham B. P.:** Writing – review & editing, Formal analysis, Conceptualization.

Declaration of Competing Interest

The authors declare that they have no known competing financial interests or personal relationships that could have appeared to influence the work reported in this paper.

Data Availability

The raw/processed data for these findings cannot be shared at this time due to technical/time limitations. However, some of the data may be made available on case-by-case basis to interested readers.

Appendix A. Material properties

Table A1
Material properties [76–78] used for the analytical model

Parameter	Ti6Al4V	IN718	H13	17–4 SS
Density, ρ (kg/m^3)	4200	7700	7100	7350
Solidus (T_S) & liquidus (T_L) temperature (K)	1878, 1923	1533, 1609	1585,1723	1677, 1713
Thermal conductivity, k (W/mK)	$8.7 \times [1 + (1.18\times10^{-3}\times T)]$	$11.5 \times [1 + (1.06\times10^{-3}\times T)]$	$22.1 \times [1 + (0.76\times10^{-3}\times T)]$	$13.7 \times [1 + (0.77\times10^{-3}\times T)]$
Specific heat, C (J/kgK)	$260 \times [1+ (1.18\times10^{-3}\times T)]$	$280 \times [1 + (1.06\times10^{-3}\times T)]$	$310 \times [1 + (0.76\times10^{-3}\times T)]$	$340 \times [1 + (0.77\times10^{-3}\times T)]$

.

Appendix B. Schematic for thermal cycle

Fig. B1 shows schematic representation of S1 strategy, and the location for calculating the thermal cycle.

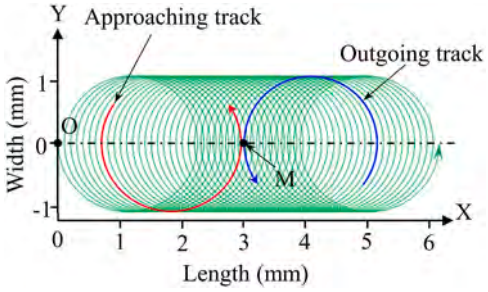

Fig. B1. Schematic representation of S1 strategy with point 'M' at 3 mm along the centerline of circular beam oscillation scanning strategy.

.

References

[1] J.L. Bartlett, X. Li, An overview of residual stresses in metal powder bed fusion, Addit. Manuf. 27 (2019) 131–149, https://doi.org/10.1016/j.addma.2019.02.020.

[2] N. Nadammal, T. Mishurova, T. Fritsch, I. Serrano-Munoz, A. Kromm, C. Haberland, P.D. Portella, G. Bruno, Critical role of scan strategies on the development of microstructure, texture, and residual stresses during laser powder bed fusion additive manufacturing, Addit. Manuf. 38 (2021) 101792, https://doi.org/10.1016/j.addma.2020.101792.

[3] E. Malekipour, H. El-Mounayri, Scanning Strategies in the PBF Process: A Critical Review, in: Vol. 2A Adv. Manuf., Proceedings of ASME 2020 International Mechanical Engineering Congress and Exposition, Virtual, Online, 2020: p. V02AT02A055. https://doi.org/10.1115/IMECE2020-24589.

[4] H. Jia, H. Sun, H. Wang, Y. Wu, H. Wang, Scanning strategy in selective laser melting (SLM): a review, Int. J. Adv. Manuf. Technol. 113 (2021) 2413–2435, https://doi.org/10.1007/s00170-021-06810-3.

[5] H. Ali, H. Ghadbeigi, K. Mumtaz, Effect of scanning strategies on residual stress and mechanical properties of Selective Laser Melted Ti6Al4V, Mater. Sci. Eng. A 712 (2018) 175–187, https://doi.org/10.1016/j.msea.2017.11.103.

[6] M. Bayat, S. Mohanty, J.H. Hattel, Multiphysics modelling of lack-of-fusion voids formation and evolution in IN718 made by multi-track/multi-layer L-PBF, Int. J. Heat. Mass Transf. 139 (2019) 95–114, https://doi.org/10.1016/j.ijheatmasstransfer.2019.05.003.

[7] L. Cao, Mesoscopic-scale numerical investigation including the influence of scanning strategy on selective laser melting process, Comput. Mater. Sci. 189 (2021) 110263, https://doi.org/10.1016/j.commatsci.2020.110263.

[8] S. Waqar, K. Guo, J. Sun, FEM analysis of thermal and residual stress profile in selective laser melting of 316L stainless steel, J. Manuf. Process. 66 (2021) 81–100, https://doi.org/10.1016/j.jmapro.2021.03.040.

[9] P. Bian, J. Shi, Y. Liu, Y. Xie, Influence of laser power and scanning strategy on residual stress distribution in additively manufactured 316L steel, Opt. Laser Technol. 132 (2020) 106477, https://doi.org/10.1016/j.optlastec.2020.106477.

[10] S. Zou, H. Xiao, F. Ye, Z. Li, W. Tang, F. Zhu, C. Chen, C. Zhu, Numerical analysis of the effect of the scan strategy on the residual stress in the multi-laser selective laser melting, Results Phys. 16 (2020) 103005, https://doi.org/10.1016/j.rinp.2020.103005.

[11] L. Parry, I.A. Ashcroft, R.D. Wildman, Understanding the effect of laser scan strategy on residual stress in selective laser melting through thermo-mechanical simulation, Addit. Manuf. 12 (2016) 1–15, https://doi.org/10.1016/j.addma.2016.05.014.

[12] W. Zhang, M. Tong, N.M. Harrison, Scanning strategies effect on temperature, residual stress and deformation by multi-laser beam powder bed fusion manufacturing, Addit. Manuf. 36 (2020) 101507, https://doi.org/10.1016/j.addma.2020.101507.

[13] J. Ning, D. Sievers, H. Garmestani, S. Liang, Analytical modeling of in-process temperature in powder bed additive manufacturing considering laser power absorption, latent heat, scanning strategy, and powder packing, Materials 12 (2019) 808–815, https://doi.org/10.3390/ma12050808.

[14] Y. Yang, F. van Keulen, C. Ayas, A computationally efficient thermal model for selective laser melting, Addit. Manuf. 31 (2020) 100955, https://doi.org/10.1016/j.addma.2019.100955.

[15] P. Zagade, B.P. Gautham, A. De, T. DebRoy, Analytical estimation of fusion zone dimensions and cooling rates in part scale laser powder bed fusion, Addit. Manuf. 46 (2021) 102222, https://doi.org/10.1016/j.addma.2021.102222.
[16] Y. Wang, X. Ji, S.Y. Liang, Analytical modeling of temperature distribution in laser powder bed fusion with different scan strategies, Opt. Laser Technol. 157 (2023) 108708, https://doi.org/10.1016/j.optlastec.2022.108708.
[17] A.J. Wolfer, J. Aires, K. Wheeler, J.-P. Delplanque, A. Rubenchik, A. Anderson, S. Khairallah, Fast solution strategy for transient heat conduction for arbitrary scan paths in additive manufacturing, Addit. Manuf. 30 (2019) 100898, https://doi.org/10.1016/j.addma.2019.100898.
[18] T. Larimian, M. Kannan, D. Grzesiak, B. AlMangour, T. Borkar, Effect of energy density and scanning strategy on densification, microstructure and mechanical properties of 316L stainless steel processed via selective laser melting, Mater. Sci. Eng. A 770 (2020) 138455, https://doi.org/10.1016/j.msea.2019.138455.
[19] E.H. Valente, C. Gundlach, T.L. Christiansen, M.A.J. Somers, Effect of Scanning Strategy During Selective Laser Melting on Surface Topography, Porosity, and Microstructure of Additively Manufactured Ti-6Al-4V, Appl. Sci. 9 (2019) 5554, https://doi.org/10.3390/app9245554.
[20] J. Robinson, I. Ashton, P. Fox, E. Jones, C. Sutcliffe, Determination of the effect of scan strategy on residual stress in laser powder bed fusion additive manufacturing, Addit. Manuf. 23 (2018) 13–24, https://doi.org/10.1016/j.addma.2018.07.001.
[21] M. Strantza, R.K. Ganeriwala, B. Clausen, T.Q. Phan, L.E. Levine, D.C. Pagan, J.P. C. Ruff, W.E. King, N.S. Johnson, R.M. Martinez, V. Anghel, G. Rafailov, D. W. Brown, Effect of the scanning strategy on the formation of residual stresses in additively manufactured Ti-6Al-4V, Addit. Manuf. 45 (2021) 102003, https://doi.org/10.1016/j.addma.2021.102003.
[22] Q. Bo, S. Yu-sheng, W. Qing-song, W. Hai-bo, The helix scan strategy applied to the selective laser melting, Int. J. Adv. Manuf. Technol. 63 (2012) 631–640, https://doi.org/10.1007/s00170-012-3922-9.
[23] X. Zhang, H. Xu, Z. Li, A. Dong, D. Du, L. Lei, G. Zhang, D. Wang, G. Zhu, B. Sun, Effect of the scanning strategy on microstructure and mechanical anisotropy of Hastelloy X superalloy produced by Laser Powder Bed Fusion, Mater. Charact. 173 (2021) 110951, https://doi.org/10.1016/j.matchar.2021.110951.
[24] H. Zhang, D. Gu, D. Dai, C. Ma, Y. Li, R. Peng, S. Li, G. Liu, B. Yang, Influence of scanning strategy and parameter on microstructural feature, residual stress and performance of Sc and Zr modified Al–Mg alloy produced by selective laser melting, Mater. Sci. Eng. A 788 (2020) 139593, https://doi.org/10.1016/j.msea.2020.139593.
[25] P. Pant, F. Salvemini, S. Proper, V. Luzin, K. Simonsson, S. Sjöström, S. Hosseini, R. L. Peng, J. Moverare, A study of the influence of novel scan strategies on residual stress and microstructure of L-shaped LPBF IN718 samples, Mater. Des. 214 (2022) 110386, https://doi.org/10.1016/j.matdes.2022.110386.
[26] A.J. Dunbar, E.R. Denlinger, J. Heigel, P. Michaleris, P. Guerrier, R. Martukanitz, T. W. Simpson, Development of experimental method for in situ distortion and temperature measurements during the laser powder bed fusion additive manufacturing process, Addit. Manuf. 12 (2016) 25–30.
[27] P. Promoppatum, S.-C. Yao, Influence of scanning length and energy input on residual stress reduction in metal additive manufacturing: Numerical and experimental studies, J. Manuf. Process. 49 (2020) 247–259, https://doi.org/10.1016/j.jmapro.2019.11.020.
[28] M.F. Zaeh, G. Branner, Investigations on residual stresses and deformations in selective laser melting, Prod. Eng. 4 (2010) 35–45.
[29] L. Mugwagwa, D. Dimitrov, S. Matope, I. Yadroitsev, Evaluation of the impact of scanning strategies on residual stresses in selective laser melting, Int. J. Adv. Manuf. Technol. 102 (2019) 2441–2450, https://doi.org/10.1007/s00170-019-03396-9.
[30] D. Wang, S. Wu, Y. Yang, W. Dou, S. Deng, Z. Wang, S. Li, The effect of a scanning strategy on the residual stress of 316L steel parts fabricated by selective laser melting (SLM), Materials 11 (2018) 1821, https://doi.org/10.3390/ma11101821.
[31] B.M. Marques, C.M. Andrade, D.M. Neto, M.C. Oliveira, J.L. Alves, L.F. Menezes, Numerical Analysis of Residual Stresses in Parts Produced by Selective Laser Melting Process, Procedia Manuf. 47 (2020) 1170–1177, https://doi.org/10.1016/j.promfg.2020.04.167.
[32] T. Machirori, F.Q. Liu, Q.Y. Yin, H.L. Wei, Spatiotemporal variations of residual stresses during multi-track and multi-layer deposition for laser powder bed fusion of Ti-6Al-4V, Comput. Mater. Sci. 195 (2021) 110462, https://doi.org/10.1016/j.commatsci.2021.110462.
[33] R.K. Ganeriwala, M. Strantza, W.E. King, B. Clausen, T.Q. Phan, L.E. Levine, D. W. Brown, N.E. Hodge, Evaluation of a thermomechanical model for prediction of residual stress during laser powder bed fusion of Ti-6Al-4V, Addit. Manuf. 27 (2019) 489–502, https://doi.org/10.1016/j.addma.2019.03.034.
[34] N.E. Hodge, R.M. Ferencz, J.M. Solberg, Implementation of a thermomechanical model for the simulation of selective laser melting, Comput. Mech. 54 (2014) 33–51, https://doi.org/10.1007/s00466-014-1024-2.
[35] E.R. Denlinger, M. Gouge, J. Irwin, P. Michaleris, Thermomechanical model development and in situ experimental validation of the Laser Powder-Bed Fusion process, Addit. Manuf. 16 (2017) 73–80, https://doi.org/10.1016/j.addma.2017.05.001.
[36] F. Dugast, P. Apostolou, A. Fernandez, W. Dong, Q. Chen, S. Strayer, R. Wicker, A. C. To, Part-scale thermal process modeling for laser powder bed fusion with matrix-free method and GPU computing, Addit. Manuf. 37 (2021) 101732, https://doi.org/10.1016/j.addma.2020.101732.
[37] H. Peng, M. Ghasri-Khouzani, S. Gong, R. Attardo, P. Ostiguy, R.B. Rogge, B. A. Gatrell, J. Budzinski, C. Tomonto, J. Neidig, M.R. Shankar, R. Billo, D.B. Go, D. Hoelzle, Fast prediction of thermal distortion in metal powder bed fusion additive manufacturing: Part 2, a quasi-static thermo-mechanical model, Addit. Manuf. 22 (2018) 869–882.
[38] C. Li, C.H. Fu, Y.B. Guo, F.Z. Fang, A multiscale modeling approach for fast prediction of part distortion in selective laser melting, J. Mater. Process. Technol. 229 (2016) 703–712, https://doi.org/10.1016/j.jmatprotec.2015.10.022.
[39] R.J. Williams, C.M. Davies, P.A. Hooper, A pragmatic part scale model for residual stress and distortion prediction in powder bed fusion, Addit. Manuf. 22 (2018) 416–425, https://doi.org/10.1016/j.addma.2018.05.038.
[40] M. Bayat, C.G. Klingaa, S. Mohanty, D. De Baere, J. Thorborg, N.S. Tiedje, J. H. Hattel, Part-scale thermo-mechanical modelling of distortions in Laser Powder Bed Fusion – analysis of the sequential flash heating method with experimental validation, Addit. Manuf. 36 (2020) 101508, https://doi.org/10.1016/j.addma.2020.101508.
[41] E. Malekipour, H. El-Mounayri, M. Marrey, E.J. Faierson, M.A. Hasan, An innovative Fast Layer-wise Simulation of Temperature distribution using a Chessboard Strategy (FALS TECHS) in the powder-bed fusion process, Addit. Manuf. 46 (2021) 102065, https://doi.org/10.1016/j.addma.2021.102065.
[42] K. Khan, L. Srinivasa Mohan, A. De, T. DebRoy, Rapid calculation of part scale residual stress – Powder bed fusion of stainless steel, and aluminum, titanium, nickel alloys, Addit. Manuf. 60 (2022) 103240, https://doi.org/10.1016/j.addma.2022.103240.
[43] P. Foteinopoulos, A. Papacharalampopoulos, K. Angelopoulos, P. Stavropoulos, Development of a simulation approach for laser powder bed fusion based on scanning strategy selection, Int. J. Adv. Manuf. Technol. 108 (2020) 3085–3100, https://doi.org/10.1007/s00170-020-05603-4.
[44] M. Masoomi, S.M. Thompson, N. Shamsaei, Laser powder bed fusion of Ti-6Al-4V parts: Thermal modeling and mechanical implications, Int. J. Mach. Tools Manuf. 118–119 (2017) 73–90, https://doi.org/10.1016/j.ijmachtools.2017.04.007.
[45] B. Cheng, S. Shrestha, K. Chou, Stress and deformation evaluations of scanning strategy effect in selective laser melting, Addit. Manuf. 12 (2016) 240–251, https://doi.org/10.1016/j.addma.2016.05.007.
[46] A. Plotkowski, M.M. Kirka, S.S. Babu, Verification and validation of a rapid heat transfer calculation methodology for transient melt pool solidification conditions in powder bed metal additive manufacturing, Addit. Manuf. 18 (2017) 256–268, https://doi.org/10.1016/j.addma.2017.10.017.
[47] W. Wang, J. Ning, S.Y. Liang, Prediction of lack-of-fusion porosity in laser powder-bed fusion considering boundary conditions and sensitivity to laser power absorption, Int. J. Adv. Manuf. Technol. 112 (2021) 61–70, https://doi.org/10.1007/s00170-020-06224-7.
[48] P.R. Zagade, B.P. Gautham, A. De, T. DebRoy, Scaling analysis for rapid estimation of lack of fusion porosity in laser powder bed fusion, Sci. Technol. Weld. Join. (2023) 1–9, https://doi.org/10.1080/13621718.2022.2164830.
[49] L. Englert, V. Schulze, S. Dietrich, Concentric scanning strategies for laser powder bed fusion: porosity distribution in practical geometries, Materials 15 (2022) 1105, https://doi.org/10.3390/ma15031105.
[50] M. Soshi, K. Odum, G. Li, Investigation of novel trochoidal toolpath strategies for productive and efficient directed energy deposition processes, CIRP Ann. 68 (2019) 241–244, https://doi.org/10.1016/j.cirp.2019.04.112.
[51] H. Yeung, J. Chen, G. Yang, Y. Guo, D. Lin, W. Tan, J. Weaver, Effect of spiral scan strategy on microstructure for additively manufactured stainless steel 17–4, Manuf. Lett. 29 (2021) 1–4, https://doi.org/10.1016/j.mfglet.2021.04.005.
[52] H. Yang, G. Jing, P. Gao, Z. Wang, X. Li, Effects of circular beam oscillation technique on formability and solidification behaviour of selective laser melted Inconel 718: from single tracks to cuboid samples, J. Mater. Sci. Technol. 51 (2020) 137–150, https://doi.org/10.1016/j.jmst.2019.09.044.
[53] Z. Wu, G. Tang, S.J. Clark, A. Meshkov, S. Roychowdhury, B. Gould, V. Ostroverkhov, T. Adcock, S.J. Duclos, K. Fezzaa, C. Immer, A.D. Rollett, High frequency beam oscillation keyhole dynamics in laser melting revealed by in-situ x-ray imaging, Commun. Mater. 4 (2023) 5, https://doi.org/10.1038/s43246-023-00332-z.
[54] H. Yeung, Z. Yang, L. Yan, A meltpool prediction based scan strategy for powder bed fusion additive manufacturing, Addit. Manuf. 35 (2020) 101383, https://doi.org/10.1016/j.addma.2020.101383.
[55] P. Gao, X. Lan, S. Yang, Z. Wang, X. Li, L. Cao, Defect elimination and microstructure improvement of laser powder bed fusion β-solidifying γ-TiAl alloys via circular beam oscillation technology, Mater. Sci. Eng. A 873 (2023) 145019, https://doi.org/10.1016/j.msea.2023.145019.
[56] R. Forslund, A. Snis, S. Larsson, Analytical solution for heat conduction due to a moving Gaussian heat flux with piecewise constant parameters, Appl. Math. Model. 66 (2019) 227–240, https://doi.org/10.1016/j.apm.2018.09.018.
[57] S.I. Kim, A.J. Hart, A spiral laser scanning routine for powder bed fusion inspired by natural predator-prey behaviour, Virtual Phys. Prototyp. 17 (2022) 239–255, https://doi.org/10.1080/17452759.2022.2031232.
[58] C. Tang, K.Q. Le, C.H. Wong, Physics of humping formation in laser powder bed fusion, Int. J. Heat. Mass Transf. 149 (2020) 119172, https://doi.org/10.1016/j.ijheatmasstransfer.2019.119172.
[59] Z. Wang, J.P. Oliveira, Z. Zeng, X. Bu, B. Peng, X. Shao, Laser beam oscillating welding of 5A06 aluminum alloys_ Microstructure, porosity and mechanical properties, Opt. Laser Technol. 111 (2019) 58–65.
[60] G. Dai, Z. Sun, Y. Li, J. Jain, A. Bhowmik, J. Shinjo, J. Lu, C. Panwisawas, Grain refinement and columnar-to-equiaxed transition of Ti6Al4V during additive manufacturing via different laser oscillations, Int. J. Mach. Tools Manuf. 189 (2023) 104031, https://doi.org/10.1016/j.ijmachtools.2023.104031.
[61] T. Mukherjee, M. Gao, T.A. Palmer, T. DebRoy, Keyhole mode wobble laser welding of a nickel base superalloy - Modeling, experiments, and process maps,

J. Manuf. Process. 106 (2023) 465–479, https://doi.org/10.1016/j.jmapro.2023.10.017.
[62] L. Wang, M. Gao, C. Zhang, X. Zeng, Effect of beam oscillating pattern on weld characterization of laser welding of AA6061-T6 aluminum alloy, Mater. Des. 108 (2016) 707–717, https://doi.org/10.1016/j.matdes.2016.07.053.
[63] Y. Chen, F. Lu, P. Nie, S.R.E. Hosseini, K. Feng, Z. Li, Dendritic microstructure and hot cracking of laser additive manufactured Inconel 718 under improved base cooling, J. Alloy. Compd. 670 (2016) 312–321, https://doi.org/10.1016/j.jallcom.2016.01.250.
[64] L. Chechik, I. Todd, Inconel 718 two ways: powder bed fusion vs. directed energy deposition, Addit. Manuf. Lett. 6 (2023) 100145, https://doi.org/10.1016/j.addlet.2023.100145.
[65] K. Khan, G. Mohr, K. Hilgenberg, A. De, Probing a novel heat source model and adaptive remeshing technique to simulate laser powder bed fusion with experimental validation, Comput. Mater. Sci. 181 (2020) 109752, https://doi.org/10.1016/j.commatsci.2020.109752.
[66] M.J. Ansari, D.-S. Nguyen, H.S. Park, Investigation of SLM process in terms of temperature distribution and melting pool size: modeling and experimental approaches, Materials 12 (2019) 1272, https://doi.org/10.3390/ma12081272.
[67] K.S. Ramani, C. He, Y.-L. Tsai, C.E. Okwudire, SmartScan: An intelligent scanning approach for uniform thermal distribution, reduced residual stresses and deformations in PBF additive manufacturing, Addit. Manuf. 52 (2022) 102643, https://doi.org/10.1016/j.addma.2022.102643.
[68] Y. Jia, C. Zeng, J. Xue, Scanning strategy optimization for the selective laser melting additive manufacturing of Ti6Al4V, Eng. Res. Express 5 (2023), https://doi.org/10.1088/2631-8695/acbd12.
[69] A.H. Nickel, D.M. Barnett, F.B. Prinz, Thermal stresses and deposition patterns in layered manufacturing, Mater. Sci. Eng. A 317 (2001) 59–64, https://doi.org/10.1016/S0921-5093(01)01179-0.
[70] L.N. Carter, C. Martin, P.J. Withers, M.M. Attallah, The influence of the laser scan strategy on grain structure and cracking behaviour in SLM powder-bed fabricated nickel superalloy, J. Alloy. Compd. 615 (2014) 338–347, https://doi.org/10.1016/j.jallcom.2014.06.172.
[71] T. Mukherjee, J.S. Zuback, A. De, T. DebRoy, Printability of alloys for additive manufacturing, Sci. Rep. 6 (2016) 19717, https://doi.org/10.1038/srep19717.
[72] K. Ren, Y. Chew, Y.F. Zhang, G.J. Bi, J.Y.H. Fuh, Thermal analyses for optimal scanning pattern evaluation in laser aided additive manufacturing, J. Mater. Process. Technol. 271 (2019) 178–188, https://doi.org/10.1016/j.jmatprotec.2019.03.029.
[73] T. Mukherjee, H.L. Wei, A. De, T. DebRoy, Heat and fluid flow in additive manufacturing – part II: powder bed fusion of stainless steel, and titanium, nickel and aluminum base alloys, Comput. Mater. Sci. 150 (2018) 369–380, https://doi.org/10.1016/j.commatsci.2018.04.027.
[74] S.A. Khairallah, A.T. Anderson, A. Rubenchik, W.E. King, Laser powder-bed fusion additive manufacturing: Physics of complex melt flow and formation mechanisms of pores, spatter, and denudation zones, Acta Mater. 108 (2016) 36–45, https://doi.org/10.1016/j.actamat.2016.02.014.
[75] T. Mukherjee, J.W. Elmer, H.L. Wei, T.J. Lienert, W. Zhang, S. Kou, T. DebRoy, Control of grain structure, phases, and defects in additive manufacturing of high-performance metallic components, Prog. Mater. Sci. 138 (2023) 101153, https://doi.org/10.1016/j.pmatsci.2023.101153.
[76] K.C. Mills, Cambridge. Recommended values of thermophysical properties for selected commercial alloys, Woodhead Publishing, 2002.
[77] R. Rai, J.W. Elmer, T.A. Palmer, T. DebRoy, Heat transfer and fluid flow during keyhole mode laser welding of tantalum, Ti–6Al–4V, 304L stainless steel and vanadium, J. Phys. Appl. Phys. 40 (2007) 5753–5766, https://doi.org/10.1088/0022-3727/40/18/037.
[78] I.R. Kabir, D. Yin, N. Tamanna, S. Naher, Thermomechanical modelling of laser surface glazing for H13 tool steel, Appl. Phys. A 124 (2018) 260, https://doi.org/10.1007/s00339-018-1671-9.